

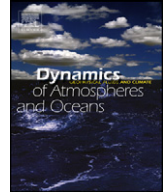


ELSEVIER

Contents lists available at SciVerse ScienceDirect

Dynamics of Atmospheres and Oceans

journal homepage: www.elsevier.com/locate/dynatmoce



Wind mediated vorticity-generation and eddy-confinement, leeward of the Madeira Island: 2008 numerical case study

X. Couvelard^{a,*}, R.M.A. Caldeira^{b,a}, I.B. Araújo^b, R. Tomé^{c,d}

^a CCM - Center for Mathematical Sciences, Universidade da Madeira, Portugal

^b CIIMAR/UP - Interdisciplinary Centre of Marine and Environmental Research, University of Porto, Portugal

^c CCMMG, University of Azores, Portugal

^d IDL, Lisbon University, Portugal

ARTICLE INFO

Article history:

Received 28 February 2012

Received in revised form 12 September 2012

Accepted 24 September 2012

Available online 4 October 2012

Keywords:

Wind-wake

Oceanic wake

Eddy containment

Madeira Island

ABSTRACT

This study assesses the influence of the atmospheric wind-wake of the Madeira Island on oceanic-eddy generation. Ocean surface wind fields derived from the QuikSCAT scatterometer were compared to the Weather Research and Forecast (WRF) modeled winds at 6km resolution. The main difference between the two wind products is found southwest of Madeira where QuikSCAT's spatial resolution [0.5°] does not resolve the near-field atmospheric wake dynamics. Nevertheless, high resolution wind extracted from ENVISAT Advanced Synthetic Aperture Radar (ASAR) confirms that WRF is able to realistically reproduce the island-induced wind-wake. The Regional Oceanic Modeling System (ROMS) was used to simulate the oceanic effects of the wind-wake. A "no-wind-wake" case was simulated with ROMS using the QuikSCAT wind, whereas the WRF wind was used for an island-induced wind-wake simulation. Oceanic surface kinetic energy and vorticity are found to increase during the summer months concurrently with strong wind-wake episodes resolved by WRF. The downstream propagation of this oceanic vorticity, as a result of the shedding of the leeward eddies, was captured with an eddy tracking algorithm. In the initial stage, the oceanic leeward eddy corridor was delimited by the zonal wind-shear. This study suggests that the wind-wake is the main contributor to the generation and containment of the oceanic eddies in the lee of the Madeira Island.

© 2012 Elsevier B.V. All rights reserved.

* Corresponding author. Tel.: +351 291 705 186.

E-mail address: xaviercouvelard@gmail.com (X. Couvelard).

1. Introduction

The role of atmospheric island wakes as a driver of oceanic mesoscale activity has recently motivated scientific discussion. Nevertheless most studies have focused on the Hawaiian Archipelago.

Calil et al. (2008) have shown that adequate wind forcing is important to reproduce the observed mesoscale vortices in the lee of the Hawaiian Archipelago. Yoshida et al. (2010) noted that the eddies observed in the southwest section of Hawaii were generated by the local wind stress curl associated with the blocking of the trade winds by the Island. Kersalé et al. (2011) emphasized the need to consider the use of high resolution wind products, i.e. QuikSCAT, in conjunction with accurate representation of the regional currents and topography in an ocean circulation model of the Hawaiian Archipelago. Furthermore they showed that high resolution winds contributed to the generation of previously studied oceanic eddies leeward of Big Island of Hawaii, whereas the Comprehensive Ocean-Atmosphere Data Set (COADS) missed important atmospheric momentum feeds to the ocean mesoscale activities. Jia et al. (2011) investigated mechanisms of eddy formation in the lee of Hawaii. In spite of showing that the interaction between the North Equatorial Current and the islands is enough to generate eddies, high resolution winds had to be considered in order to reproduce the level of kinetic energy and eddy occurrences observed by altimetry.

Wind generated eddies have also been identified in the wake of Mindoro and Luzon Island in the Philippines where the incoming oceanic flow was found to be inhibited by the local geography (Pullen et al., 2008). This effect supports numerical results discussed by Dong and McWilliams (2007) for the South California Bight, where wind driven shear flow between the islands contributed significantly to the generation of local vorticity, while the wind curl leeward of the islands generated vorticity strips through Ekman pumping. While all these studies highlight the importance of the wind forcing in eddy generation, two-dimensional numerical studies of the Gran Canaria region (Jimenez et al., 2008), have suggested that the local generation of oceanic eddies is mainly forced by topographic perturbation to the oceanic flow, while the wind mainly acts as an energy contributor to the oceanic vorticity. This was partially confirmed by Piedeleu et al. (2009) when comparing the wind variability with the occurrence of cyclonic eddies using data from a mooring leeward of Gran Canaria Island.

Madeira is a volcanic Island located north of the Canary Islands (32.5°N ; 17°W), ~ 700 km from the African continent and ~ 850 km from the Iberian Peninsula (Fig. 1). The island orography has a mountain range positioned across its length, aligned perpendicularly to the incoming NE trade winds. In contrast to other archipelagos mentioned herein, Madeira's neighboring islands have small mountains (<300 m) which are well below the atmospheric inversion layer and therefore they do not strongly affect the atmospheric wake of the main island. The atmospheric wake generated by the main island is a clear feature in satellite images (Fig. 2). The interaction between the mountains and the NE winds,

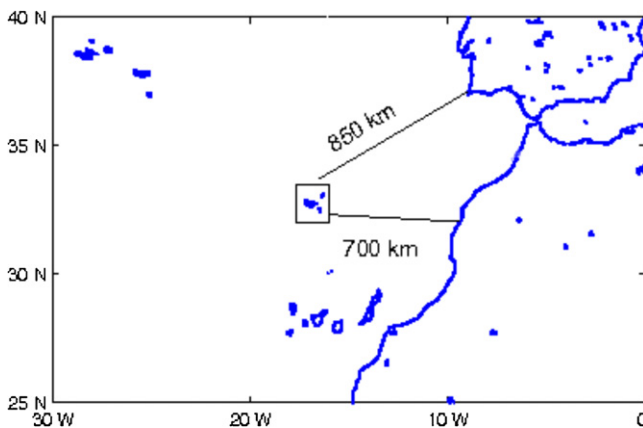


Fig. 1. Location in the north east Atlantic of the Madeira Archipelago (islands showed in small box) with distances to the African continent (cc 700 km) and south west Iberian peninsula (cc 850 km).



Fig. 2. Atmospheric manifestation of a Von Karman Vortex Street (VKVS) in the lee of Madeira Island, captured by MODIS-terra. Image acquired on the 5 July 2002. Credit: Jacques Desclotres, MODIS Land Rapid Response Team, NASA/GSFC (<http://visibleearth.nasa.gov/>). The cloud wake of Madeira, can be seen extending south of Canaries Island, more than 1000 km leeward.

in conjunction with the fact that the atmospheric inversion layer is often below the mountain top (1590–1862 m), favors the formation of strong atmospheric wake episodes, which is frequently manifested as Von Karman Vortex Streets (VKVS). Since satellite images of the Madeira VKVS have become available, they have inspired studies such as Moll (1971), Scorer (1986) and Etling (1989). Remote sensing based studies have shown evidence of the regular presence of atmospheric and oceanic wakes on the lee of the archipelago, including the shedding of oceanic eddies (Caldeira et al., 2002; Araújo et al., 2010; Caldeira and Sangra, 2012).

The atmospheric wake generated by the mountain range across the Island of Madeira (25 km wide and 50 km long) will not be adequately resolved by most of the freely available wind products and will therefore underestimate its oceanic effect. However the near-field implications of atmospheric wake need to be accurately resolved. In the case of Hawaii, Calil et al. (2008) forced an ocean model

by QuikSCAT [25 km] and MM5 winds [9 km]. They showed that the near-field wind was correctly resolved by QuikSCAT, which was then used as a high resolution wind product in some other Hawaiian wind-wake studies (Kersalé et al., 2011; Jia et al., 2011).

In the case of Canary Islands, Jimenez et al. (2008) has considered an averaged constant wind-stress curl induced by a vertical cylinder-like island and so did not take account of mountain geometry and wind variability.

To better represent the implication of the near-field wind in the case of Madeira, an atmospheric model was employed. QuikSCAT wind [0.5°] has been used as a reference “no wind-wake”. Particular attention was given to the wind-wake influence in the (i) generation and (ii) downstream containment of oceanic eddies. Several wake episodes were identified by multiple satellite sensors during 2008 (Araújo et al., 2010) and so the discussion is focused on this year.

The present paper is structured as follows: in Section 2, data and model configurations are detailed; complementary numerical tools and analysis are also explained here. Section 3 compares the atmospheric model wind solutions with satellite derived wind products; the main discussion thereafter focuses on the effect of wind-forcing on the generation and containment of wake-eddies. Section 4 summarizes the main results.

2. Materials and methods

Satellite derived wind products and numerical models have been used in order to assess the role of atmospheric wind forcing on the generation and propagation of oceanic eddies.

The Weather Research and Forecasting Model (WRF), with boundary and initial condition from ECMWF ERA Interim re-analysis was used to calculate an accurate representation of island-modified winds. The Regional Ocean modeling System (ROMS) was used to represent the ocean dynamics, whereby island-modified wind effects (WRF forcing) as well as no-island modified winds (QuikSCAT forcing) were both considered in its simulations. The downstream fate of oceanic eddies was studied with a well documented eddy-tracking algorithm (Nencioli et al., 2010).

2.1. Satellite derived winds

Satellite wind speed and direction were obtained from QuikSCAT daily gridded wind products extracted from CERSAT (<http://www.ifremer.fr/cersat>) and from ENVISAT's Advanced Synthetic Aperture Radar (ASAR) extracted from SOPRANO-CLS (<http://soprano.cls.fr>).

2.1.1. QuikSCAT data

The wind scatterometer has been adopted as a standard instrument to measure near surface wind vectors over the ocean (Stoffelen and Anderson, 1997).

QuikSCAT derived winds are considered an accurate representation of oceanic winds, and have therefore been used to force regional ocean circulation models (e.g. Chelton et al., 2006; Calil et al., 2008; Kersalé et al., 2011; Jia et al., 2011). Moreover the use of QuikSCAT wind products allows for an accurate representation of the synoptic regional variability, when compared to climatological winds from the Comprehensive Ocean-Atmosphere Data Set (COADS).

In a numerical study of mesoscale eddies leeward of Hawaii, Calil et al. (2008) showed that the main regional oceanic features were well reproduced in their oceanic model using both COADS and QuikSCAT climatologies. However, when using QuikSCAT winds a more realistic representation of oceanic vorticity and kinetic energy was achieved. This product has therefore been selected to reproduce mesoscale eddies in the lee of the archipelago (e.g. Jia et al., 2011; Kersalé et al., 2011).

Madeira is substantially smaller than the Hawaiian Archipelago. Therefore the initial stages of oceanic eddy formation are expected to act on scales well below the Rossby radius of deformation (R_d), which is estimated at 22 km (Chelton et al., 1998). This scale is just under QuikSCAT's spatial resolution. Furthermore the wind resolution is known to be compromised at the submesoscale and/or near the (islands) coast, which means that this product is inadequate to resolve the Madeira Island-induced curl. In this sense, we have chosen to use QuikSCAT wind to force a “no-wind-wake” oceanic case simulation.

Notwithstanding the above discussion, it is generally accepted that QuikSCAT data is an accurate representation of the daily mean wind speed and direction (Chelton et al., 2006), and thus can be used with some confidence as reference data to validate regional wind speed and direction. For these reasons this study also uses QuikSCAT winds away from the coast and wake area, since they provide the highest temporal resolution dataset.

Wind speed and direction was derived from radar backscatter. CERSAT reconstruction of gap-filled and averaged synoptic fields is achieved through a statistical interpolation. Wind divergence and stress curl are also derived from wind and wind stress respectively. The advantage of this product over the European Remote Sensing (ERS) satellite and NASA Scatterometer (NSCAT) is the higher spatial resolution (Stoffelen and Anderson, 1997).

2.1.2. Advanced Synthetic Aperture Radar (ASAR)

The coarse and limited coastal resolution of the scatterometer, which was mentioned earlier, have contributed to a growing interest in the use of data collected from Synthetic Aperture Radar (SAR) sensors for mapping wind (10 m) at a high spatial resolution (1–10 km).

The ENVISAT ASAR data (hereafter referred to SAR data) were provided by the European Space Agency (ESA) and processed by SOPRANO-CLS. Wind speed and direction was extracted from the Wide Swath Mode (WSM) product (400 km), which has sufficient spatial resolution to capture Madeira's atmospheric wake (near-field) features.

The SAR wind retrieval techniques are designed to extract the 10 m neutral equivalent surface wind. The resolution of the processed wind is [975 m × 975 m]. Note that caution is needed when analyzing results for winds <2 m s⁻¹ or above 20 m s⁻¹. Soprano-CLS method for wind vector retrieval combines a statistical (Bayesian) approach (Portabella et al., 2002; Kerboal, 2007), with an auxiliary model data (ECMWF), in order to obtain the best estimate of speed and direction. The Bayesian wind speed estimate achieves a root-mean square (RMS) error of 1.87 m s⁻¹ for 2–20 m s⁻¹ wind speed range, which is a 20% improvement over the classical scatterometer approach. This error is significantly reduced for average wind speed ranges of 5–9 m s⁻¹.

2.2. WRF-ARW model setup

The present study uses version 3.2 of the Advanced Research Weather and Forecasting Model (WRF-ARW) (Skamarock et al., 2008) with one-way nested domains at 54, 18 and 6 km horizontal grid resolutions. The top layer of the model is located at 50 hPa and a total of 31 vertical levels were used. All grids use: (i) NOAA Land Surface Model (Chen and Dudhia, 2001); (ii) the Rapid Radiative Transfer GCM (RRTMG) scheme for long and shortwave radiation (Mlawer et al., 1997); and (iii) and the WSM 6-class graupel scheme (Lin et al., 1983; Hong et al., 2004) for the cloud physics. The Mellor–Yamada–Janjic TKE scheme (Janjic, 1990, 1996, 2002) is used for the Planetary Boundary Layer and the Betts–Miller–Janjic (Janjic, 1994, 2000; Betts, 1986; Betts and Miller, 1986) cumulus scheme is employed in the 54 and 18 km grids. The initial and time dependent boundary conditions for the outer domain were derived from the ECMWF-ERA Interim re-analysis product (Dee et al., 2011).

Fig. 3 (top) shows a representation of the WRF-ARW nested domains. The 54 km resolution domain (black) is propagated into an 18 km resolution intermediate domain (blue). The results from the regional (6 km) nested solution (green) were used to force the ocean circulation model. Preliminary sensitivity analysis (not shown) suggested that 6 km was the minimum WRF resolution needed, in order to adequately resolve the island-induced wind-wake. Larger domain sizes and/or higher resolutions demand unmanageable computational resources. Therefore a compromise between disk-space and computing-time was necessary to avoid jeopardizing the model's ability to represent the processes discussed herein.

2.3. ROMS experimental setup

The ocean circulation model used in this study was the Regional Oceanic Modeling System (ROMS-Agrif, <http://www.romsagrif.org/>) described in detail in Shchepetkin and McWilliams (2003, 2005). ROMS is a split-explicit, free-surface and terrain-following vertical coordinate oceanic model, where

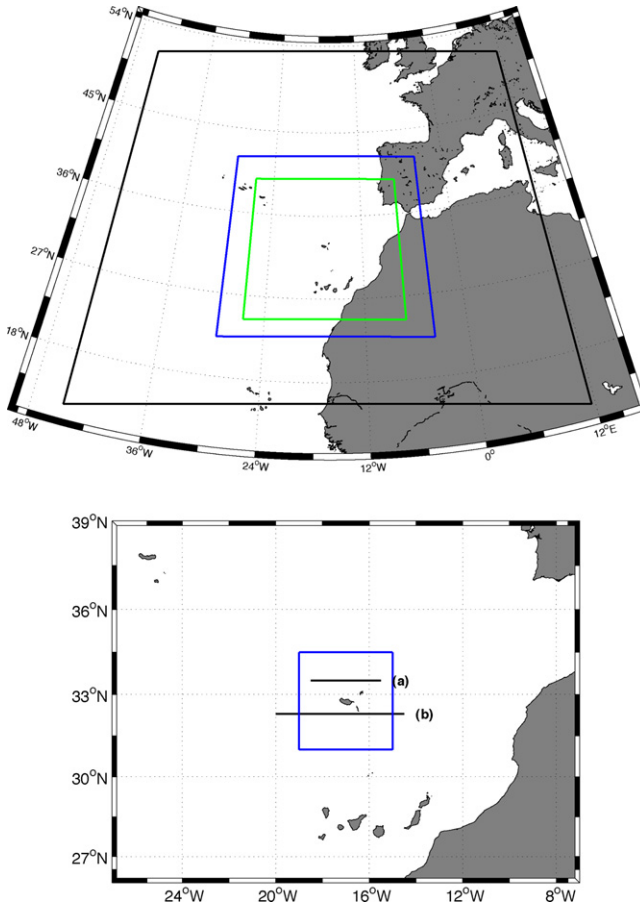


Fig. 3. WRF nested model domains. Top-panel: the black line represents the outer domain forced by the ECMWF ERA Interim re-analysis product at 54 km; blue-line represents the intermediate domain at 18 km; and the green-line represents the regional 6 km model domain, used to forced the ocean circulation model. Bottom-panel: in blue, area use for average KE and vorticity presented in Figs. 12 and 13, black lines (a) and (b) indicate sections shown in Figs. 6, 7 and 11. (For interpretation of the references to color in this figure legend, the reader is referred to the web version of the article.)

short time steps are used to advance the surface elevation and barotropic momentum equation, and a larger time step is used for temperature, salinity, and baroclinic momentum. ROMS employs a two-way time-averaging procedure for the barotropic mode which satisfies the 3D continuity equation. The specially designed predictor–corrector time-step algorithm allows a substantial increase in the permissible time-step size. The third-order, upstream-biased, dissipative advection scheme for momentum allows the generation of steep gradients, enhancing the effective resolution of the solution for a given grid size (Shchepetkin and McWilliams, 1998). For tracers, the RSUP3 scheme where diffusion is split from advection and is represented by a rotated geopotential biharmonic diffusion scheme (Marchesiello et al., 2009), in order to avoid excessive spurious diapycnal mixing associated with sigma coordinates, is used. Explicit lateral viscosity is null everywhere in the model, except in sponge layers near the open boundaries where it increases smoothly on several grid points. A K-Profile Parameterization (KPP) boundary layer scheme (Large et al., 1994) accounts for the subgrid-scale vertical mixing processes.

The model grid, the atmospheric forcing, the initial and boundary conditions were all built using an adapted version of the ROMSTOOLS package (Penven et al., 2007). The bottom topography is derived

from the GEBCO 30" resolution database (www.gebco.net). Despite the current implementation of a new pressure gradient scheme associated to a modified equation of state that limits computational errors of the pressure gradient (Shchepetkin and McWilliams, 2003), the bathymetry still needs to be smoothed, so that the slope parameter $r = \Delta h / 2h$ (Beckmann and Haidvogel, 1993) remains lower than 0.2. To ensure acceptable resolution of the upper ocean, we use 35 vertical levels with stretched s -coordinates, using surface and bottom stretching parameters $\theta_s = 6$, $\theta_b = 0$ respectively (Song and Haidvogel, 1994). At the lateral boundaries facing the open ocean, a mixed passive-active, implicit, radiation condition connects the model solution to the surroundings (Marchesiello et al., 2001).

ROMS was initialized and forced at the oceanic boundaries, by temperature and salinity profiles extracted from the World Ocean Atlas climatology (Locarnini et al., 2006; Antonov et al., 2006). Atmospheric fluxes (heat and water) were extracted from COADS and introduced in the ocean model through the bulk formulae (Fairall et al., 2003). The model domain extends from -22.5° to -12°E and from 30° to 35.5°N , on a $1/18^\circ$ (~ 5 km) regular grid. The ocean model results discussed herein were extracted after the volume averaged kinetic energy reaches a steady-state (two year spin-up period). This setup was used in two numerical experiments: a control experiment using daily mean wind extracted from QuikSCAT and an experiment using daily mean wind, calculated with WRF-ARW.

2.4. Eddy-tracking algorithm

In order to study the role of the wind in mediating the tracks of the oceanic eddies downstream of the island, some concurrent eddy position and wind conditions were taken into consideration. The "Vector Geometry-Based Eddy Detection Algorithm" (Nencioli et al., 2010) was adopted to be used with the ROMS output. This algorithm represents an alternative to other existing approaches using Okubo–Weiss Parameter (Chelton et al., 2007), wavelet analysis (Doglioli et al., 2007) or the winding angle method (Chaigneau et al., 2008). To identify an eddy the algorithm assumes that: (i) along an east–west section, the sign of the meridional velocity [v] has to reverse across the eddy center, and its magnitude has to increase away from it; (ii) along a north–south section, the sign of the zonal velocity [u] has to reverse across the eddy center and its magnitude has to increase away from it while the sense of rotation has to remain the same as [v]; (iii) the velocity magnitude has a local minimum at the eddy center; and (iv) around the eddy center the direction of the velocity vectors have to change with a constant sense of rotation. For a detailed description, refer to Nencioli et al. (2010). Two parameters need careful consideration: (i) [a], which defines how many grid points are used to search for [u , v] reversals, and (ii) [b], which is the number of grid points of the search area used to define the local velocity minimum. Although a slightly lower grid resolution than that used in Nencioli et al. (2010) case study was used here (5 vs 1 km respectively), a few sensitivity experiments (not shown) have shown that the same parameters ($a = 4$ and $b = 3$) were also adequate for this Madeira wake study.

3. Results and discussion

The role of the wind in the generation of wake eddies in the area has not received much attention in the scientific literature. To evaluate the impact of the wind-induced wakes in the generation of oceanic wakes, while considering the size, orientation and atmospheric impact of Madeira orographic flows, several new aspects needed careful attention. Firstly, the near-field (island coast / flanks) atmospheric vorticity must be accurately depicted by the wind product, i.e. sufficient spatial resolution. Secondly, the wind product needs to have enough temporal resolution to allow for the study of a substantial portion of the life cycle of wind-induced oceanic structures (e.g. eddies). Thirdly, the effects of the transfer of atmospheric momentum onto the ocean surface, i.e. conversion of wind-stress curl in oceanic vorticity through, upwelling and downwelling induced by surface wind shear (Patzert, 1969; Jia et al., 2011) must be accurately represented. Finally, there must be an accurate method of concurrently monitoring the wind and oceanic variability, in order to be able to study the continuous role of the wind effect on oceanic features further downstream.

To address these points wind products were first compared and cross-validated to guarantee a faithful representation of the atmospheric (island-induced) vorticity. Next, the sea surface manifestation of atmospheric wake was considered in terms of surface vorticity and KE, including the study

of its intra-annual variability. Finally a case study of the wind-induced confinement of oceanic eddies was carried out, in order to determine whether the island-modified wind would continue to influence the oceanic downstream region.

3.1. Resolving the atmospheric wake – comparing wind products

Mean winter wind speeds for WRF and QuikSCAT are shown in Fig. 4(a) and (b) respectively. WRF was able to reproduce a small north/south symmetric wind-wake while QuikSCAT did not produce any. In Addition differences were also found between the wind products when the Root Mean Square Deviation (RMSD) of wind speed and direction was examined, as shown in Fig. 4(c) and (d) respectively. While differences in wind speed are maximum close to Madeira, maximum differences in wind direction extend from the island as far as the southern limit of the domain.

In contrast, the WRF summer mean wind speed (Fig. 5(a)) shows a strong wind-wake extending almost 300 km south of Madeira characterized by the low wind (~ 100 km extension) seen south of the island adjacent to 2 bands of strong wind characteristic of the shear layer. Comparatively, QuikSCAT wind speeds (Fig. 5(b)) throughout the domain are found to be very similar to WRF winds except that the wind-wake is absent in the satellite wind product.

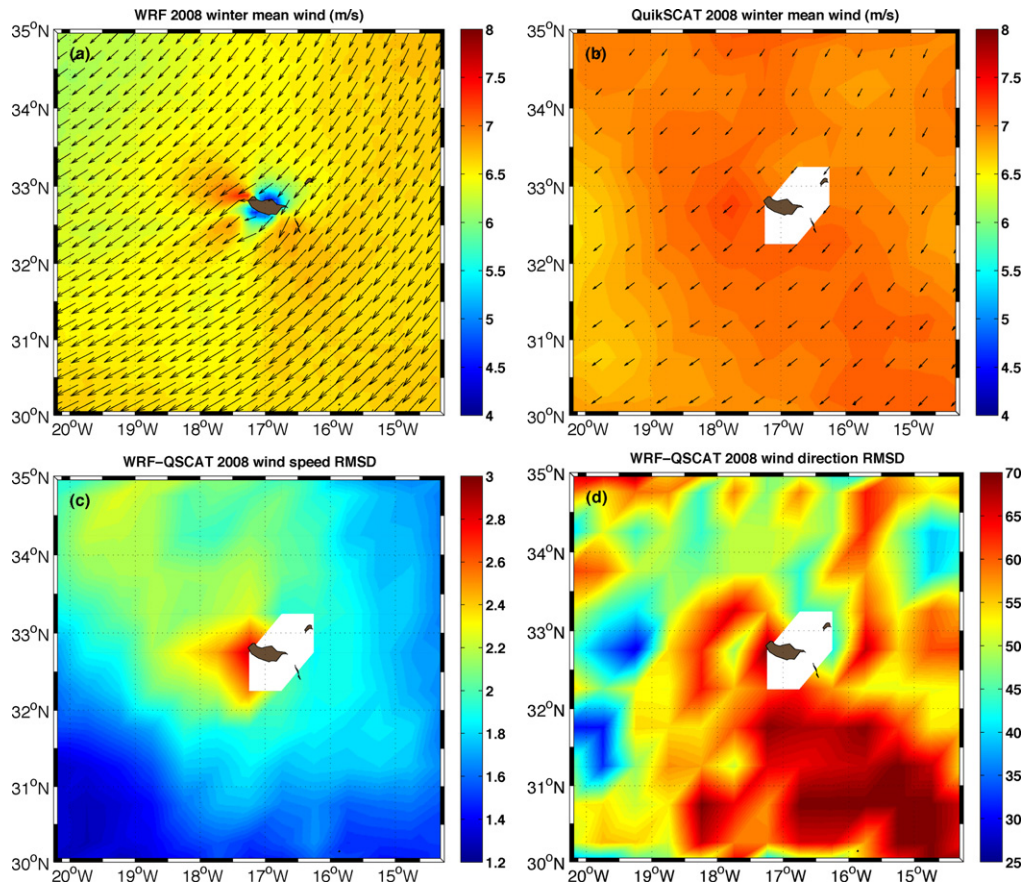


Fig. 4. Top-panels: mean winter wind speed for WRF (a) and QuikSCAT (b) (black arrow represents wind direction; one arrow every 4 point for WRF, one every point for QuikSCAT). Bottom-panels: Root Mean Square Deviation (RMSD) between WRF and QuikSCAT wind speed (c) and direction (d) for the winter 2008. White area represents to the QuikSCAT landmask.

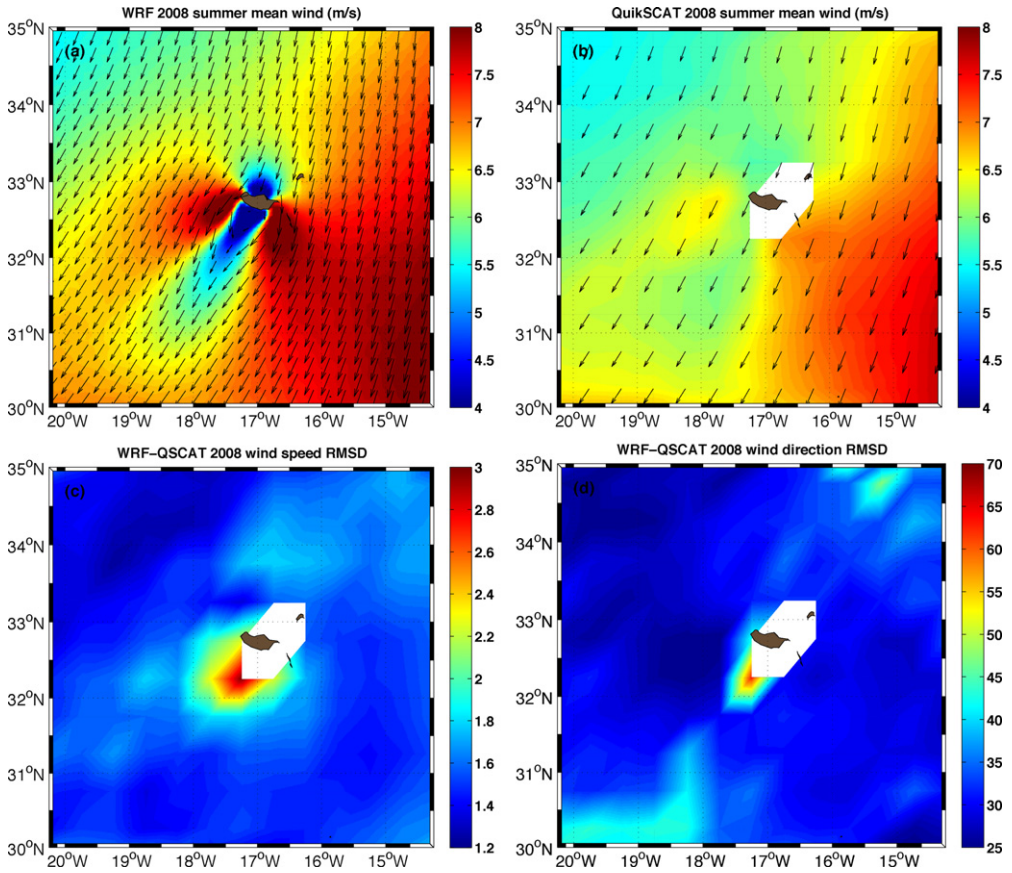


Fig. 5. Top-panels: mean summer wind speed for WRF (a) and QuikSCAT (b) (black arrow represents wind direction; one arrow every 4 point for WRF, one every point for QuikSCAT). Bottom-panels: Root Mean Square Deviation (RMSD) between WRF and QuikSCAT wind speed (c) and direction (d) during the summer 2008. White area represents to the QuikSCAT landmask.

Summer wind speed RMSD (Fig. 5(c)) immediately southwest of the island are large, i.e. between 2 and up to 3 m s^{-1} , while away from the island it is lower than 1.6 m s^{-1} and more uniform. Larger differences (up to 60°) in wind direction are also found southwest of the island (Fig. 5(d)). Elsewhere, differences are of the order of 25° . Mean Absolute Differences (not shown), which are comparable to the RMSD analysis, reflect a low variance of the differences around the mean deviation. This suggests a low temporal and spatial dispersion of the differences compared to the average. These results show that except toward the leeward side of Madeira, WRF and QuikSCAT regional wind products are very similar, especially during the summer months. Nevertheless QuikSCAT is unable to reproduce the atmospheric wake induced by the Island.

QuikSCAT and WRF wind speed and direction are averaged along a transect ($15.5\text{--}18.5^\circ\text{W}$, at 33.5°N , Fig. 3, section (a)), windward of Madeira Island. Results are shown in Fig. 6, where 0.79 and 0.81 correlation coefficient were obtained for wind speed and direction, respectively, confirming that both products are generally similar and able to represent the predominant trade winds found during the summer. However these results are no longer valid when analyzing wind variability leeward of Madeira Island, i.e. considering the orographic effect on the wind.

A Hovmöller diagram (longitude-time, Fig. 7), representing the wind regime south (leeward) of Madeira at 32.3°N (Fig. 3, section (b)), reveals an area of low wind centered at 17°W (center of Madeira Island) almost omnipresent throughout the 2008 WRF solutions (left panel). This low wind

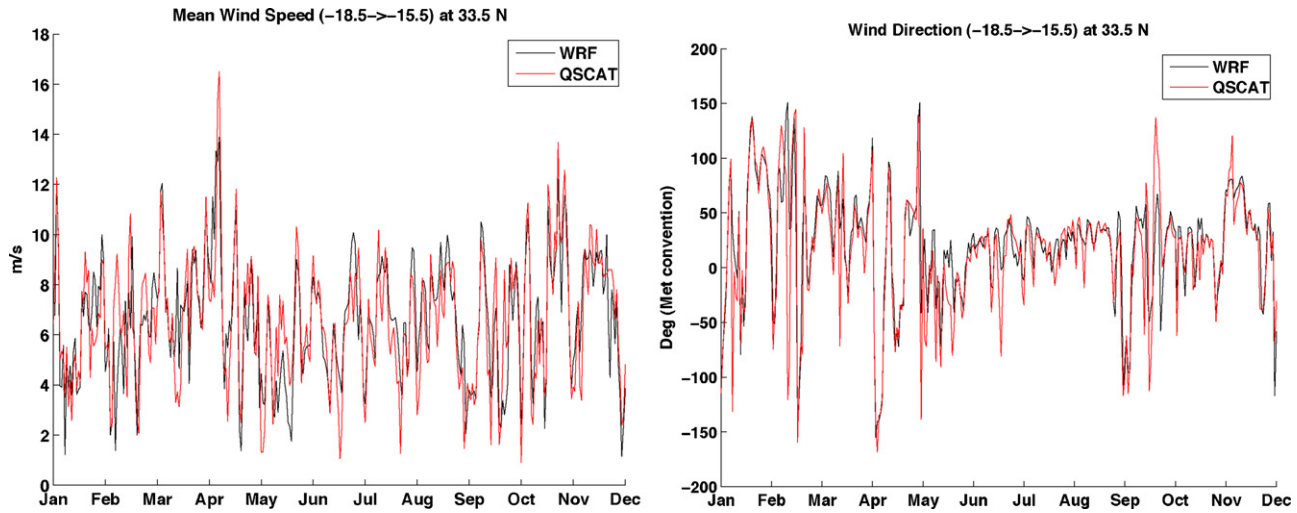


Fig. 6. Wind Speed (left-panel) and direction (right-panel) from WRF (black line) and QuikSCAT (red) averaged between 18.5°W and 15.5°W at 33.5°N (north of Madeira, line (a) of Fig. 3). This illustrates the similarity of the incoming wind between the two products for the trades wind period (May–September). Wind direction between -90° and 90° correspond to the north quadrant (0° = north wind, 45° = northeast winds). (For interpretation of the references to color in this figure legend, the reader is referred to the web version of the article.)

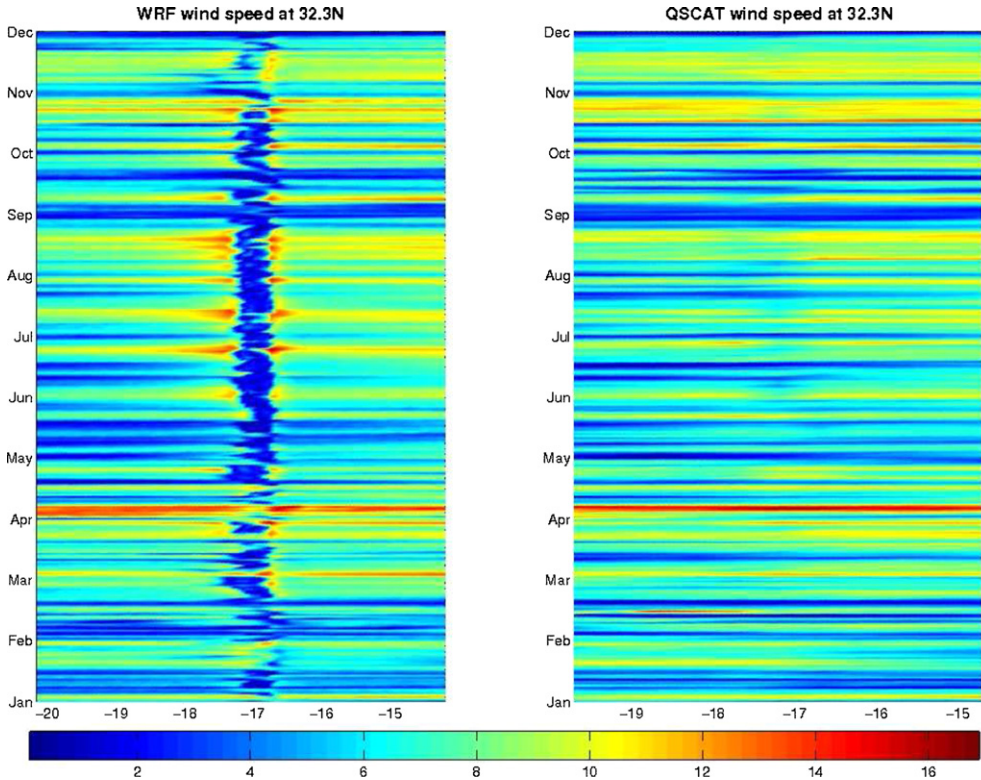


Fig. 7. Hovmöller diagram of wind speed (m s^{-1}) extracted from WRF (left-panel) and QuikSCAT (right-panel) at 32.3°N (south of Madeira, line (b) of Fig. 3). In the WRF case an almost permanent zone of low wind can be identify at 17°E , with a strong intensification between June and August. Comparison between both diagrams shows that WRF reproduce the far-field variability of the wind, as depicted by QuikSCAT.

signal is representative of the wind-wake signature which is absent in the QuikSCAT wind (right panel). This diagram also shows the intensification of the wake during the summer months, concurrent with the seasonal occurrence and intensification of the trade winds (Fig. 6). During the summer months, an intensification of the wind on the east–west flanks of the islands forms shear-layers with strong wind curl (further discussed below). It is also interesting to note that the intra-annual wind variability revealed by QuikSCAT (right panel of Fig. 7) is also well reproduced by WRF. For instance stronger winds during April and weaker winds during September are also depicted by the atmospheric model.

Notwithstanding the fact that WRF wind is used in a realistic configuration forced by reanalyzed data, there was still a need to assure a realistic representation of the atmospheric wake. In this regard WRF simulated winds were compared with SAR derived winds. SAR (cf. Section 2.1) wind data allowed the reconstitution of the wind speed and direction at resolution of ~ 1 km. Although few synoptic SAR images of the wind-wake are available, these are not affected by land contamination and therefore can be used to detect the near-field wake changes in wind. It was also used to validate WRF solutions. From a total of twelve available SAR images processed for 2008, four images (April, August, October and December) captured a wake episode south of Madeira. Particularly interesting images (centered on the wake) found in August and October were selected and compared with WRF. Although October was not included in our definition of summer, the north-east wind conditions seen in Fig. 6 (left) and low wind region in Fig. 7 make this case characteristic of a summer month leeward wake and have therefore been considered for the WRF validation.

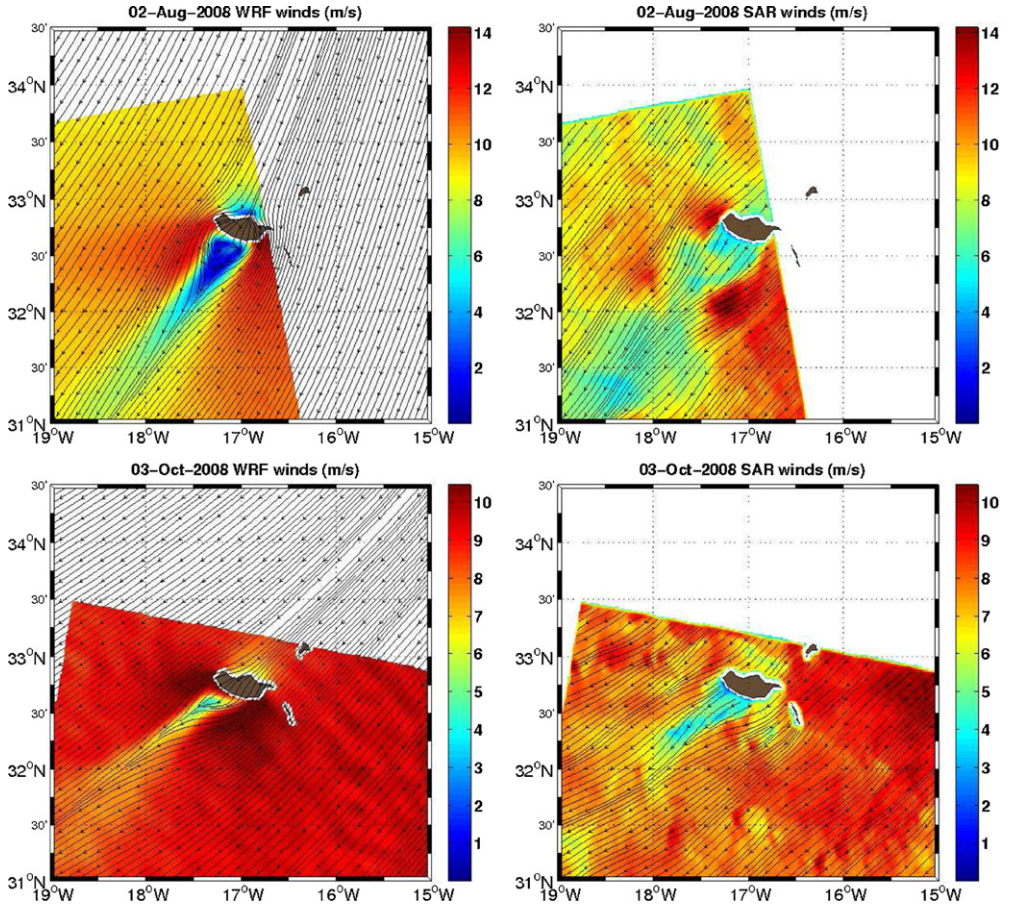


Fig. 8. Wind-wake, as calculated by WRF (left-panels) and measured by SAR (right) for two different dates (2nd of August, and 3rd of October 2008) showing the characteristics trade incoming winds. For this comparison both SAR and WRF have been interpolated in a 1 km regular grid and WRF wind is only plotted where SAR is available. The streamline are represented in black.

Fig. 8 shows WRF (left) and SAR (right) wind speed for two different dates (August the 2nd and October the 3rd 2008), with both being interpolated onto a 1 km regular grid. Unnecessary detail in the SAR wind data was eliminated by applying a $[7 \times 7]$ km averaged filter, without compromising the wake signature. To aid comparison, WRF wind speed is only represented over the SAR track, while streamlines cover the entire figure. As expected the atmospheric wake region has recirculation cells with weaker return flows. However wakes represented by WRF solutions are symmetrical, in contrast to the wakes represented by the SAR data. Nevertheless it is important to consider that WRF solutions are daily means at 6 km resolution, i.e. they represent an average state over several shedding periods, while SAR derived products represent snapshots at certain times. At its worst the WRF solution only underestimates the leeward length and the very fine detail of the near-field wake. SAR captures atmospheric wakes extending further south and slightly wider than those reproduced by WRF. Considering the overall direction, length and intensity, both SAR and WRF wake are comparable, reinforcing the notion that WRF can realistically simulate the near-field turbulent region characterizing wakes events. It is also noteworthy that SAR derived wind speed values are in the range of SAR accurate reproducibility (>2 and <20 m s^{-1} , cf. Section 2.1).

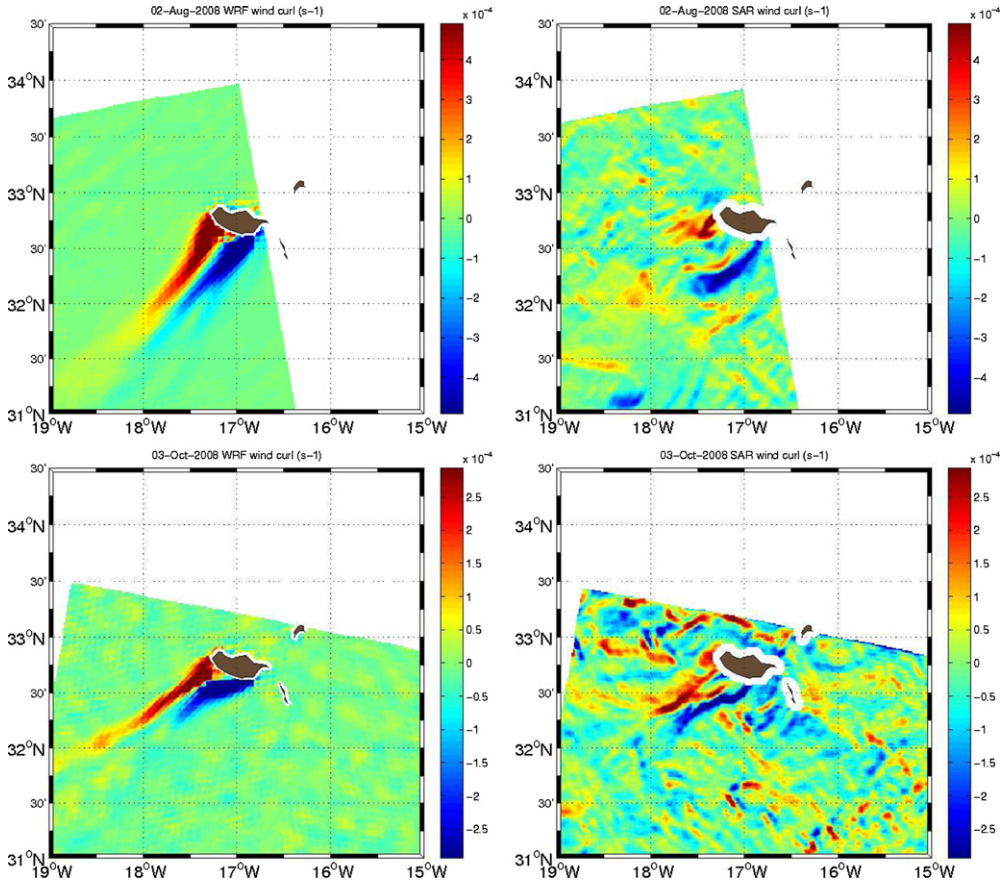


Fig. 9. The vertical component of the wind curl, as calculated by WRF (left) and derived from SAR (right) for the 2 of August 2008 (top) and the 3 October 2008, characteristic of trade incoming winds. SAR wind curl was computed after a 7 km averaged filter was applied on the wind.

The vertical component of the wind curl ($(\vec{\nabla} \times \vec{U}) \cdot \vec{k}$) for the August and October events is presented in Fig. 9. WRF results show a symmetric positive and negative curl with the cyclonic component being more developed than its anticyclonic counterpart (Fig. 9, left). Furthermore, the anticyclonic curl obtained from SAR and WRF are comparable, indicating that WRF is able to capture the orographically induced variability of the near-field atmospheric wake. The asymmetry in the wind curl found in SAR, in contrast with WRF, can be explained by the mountain's geometry (Wide plateau on the west, Paul da Serra (~1500 m); high and steep mountainous peaks on the east, Pico Ruivo and Arieiro (~1800 m), which, at the current resolution is not fully well represented in WRF.

Despite some suggestion of a slight overestimation in the cyclonic vorticity of WRF when compared to that in SAR and taking into account that daily WRF output at 6 km resolution (inducing a smoothed Madeira Relief) is being compared with a ~1 km resolution instant satellite product, these results are however indicative that the atmospheric model adequately resolves most aspects of the wake.

Future studies should consider higher temporal and spatial resolution WRF simulations, in order to accurately reproduce the very fine wake details. Recent ongoing work (unpublished) that compares WRF high resolution simulations (i.e. 1 km; hourly), with airborne data during a Madeira atmospheric wake event show improvements in the reproduction of the fine wake details. Furthermore diabatic aspects and two-way coupling between atmosphere and oceanic models also need to be considered

for the most accurate representation of the ocean feedback mechanisms, which seem to also play a role in these wind-induced events (e.g. Pullen et al., 2005, 2007; Small et al., 2008).

The scales and mechanisms of the Island wake seem similar to those of Bora wind events (Signell et al., 2010). Bora winds are orographic induced jets which propagate over the Adriatic ocean, analogous to the jets generated in the flank of a mountainous island. Signell et al. (2010) used SAR images collected during a Bora event to study the wind field and showed unprecedented results, which were unresolved by other wind products such as COADS and mesoscale meteorological models such as the Coupled Ocean Atmosphere Mesoscale Prediction System (COAMPS). Compared to SAR, the 4 km mesoscale meteorological and/or coupled models did not resolve accurately the very fine details such as the dual-jet nature of some of the Bora winds. Thus it is likely that sub-kilometer models are required to further improve the reproducibility of the near-field physics. Furthermore ocean surface heat fluxes were also shown by Pullen et al. (2007) to play an important role in the modulation of Bora events. Nevertheless the active nature of the SAR sensor requires it to be switched off over oceanic areas, unless there are specific approved requests for the data. This explains why the comparative study discussed herein is a priori limited to the study of episodic events.

3.2. Wind-induced oceanic response

The study on the oceanic response to the atmospheric island wake considered two specific scenarios: a case where the island generate a wind-wake and a case where it does not. Thus far we have shown that the wind-wake is well represented by WRF, but not by QuikSCAT wind products. Therefore we used the latter to force a “no-wake” case in contrast to a “wake” case, forced by the WRF wind product. This involved two ocean model simulations using identical oceanic boundary and initial conditions (cf. Section 2.3).

Analysis of the results focuses on the transfer of momentum from the atmosphere to the ocean considering the oceanic vorticity and kinetic energy generated in these two scenarios.

3.2.1. Surface vorticity and kinetic energy

Fig. 10 shows the WRF and QuikSCAT mean summer wind stress curl induced by Madeira orography. The WRF results show the generation of positive and negative vorticity in the island’s flanks which is expected to have a significant oceanic impact. The ocean model forced by WRF (wind-wake case) is therefore expected to have a different sea surface vorticity scenario relative to the model forced with QuikSCAT (no-wind-wake case).

A mean summer vorticity profile for a transect leeward of Madeira Island (32.5°N) is shown in Fig. 11. The oceanic impact of the WRF wind-stress curl on the generation of near-field oceanic

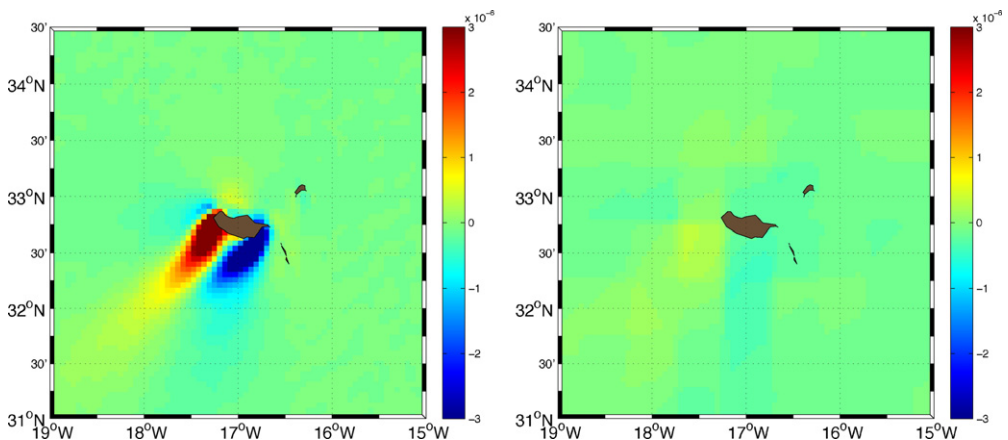


Fig. 10. Summer mean wind stress curl (N m^{-3}) for WRF (left-panel) and QuikSCAT (right-panel).

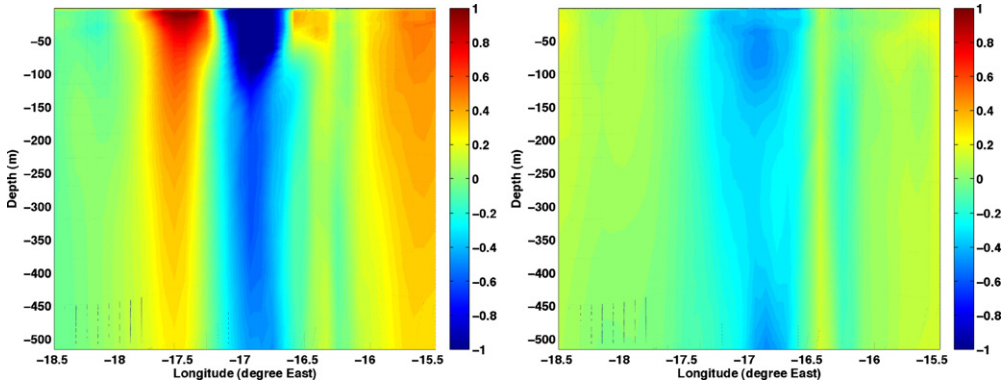


Fig. 11. Mean summer profile of oceanic vorticity (10^{-5} s^{-1}), in a latitudinal transect leeward of Madeira (32.3° N , line (b) of Fig. 3). Left-panel: WRF forced ROMS. Right-panel: QuikSCAT forced ROMS

vorticity is greater than for QuikSCAT forcing. It is also interesting that in both cases there is an asymmetry between cyclonic and anticyclonic vortices. Furthermore in the WRF case oceanic vorticity is concentrated in the upper 100 m. Anticyclonic vorticity is also substantially weaker when using QuikSCAT forcing (no wind-wake). The western oceanic flank of Madeira has a wider island-shelf compared to the narrow and steep ridge of the eastern flank. Thus the resulting oceanic vorticity should reflect some interaction between surface currents and frictional damping, which can be induced by the topography (island shelf) or by a strongly stratified upper layer ($Bu = (NH/fL)^2 \sim 1$ (Cushman-Roisin, 1994), where Bu is the Burger number, N is the buoyancy frequency, H the vertical scale of the flow, f the planetary vorticity and L is the horizontal scale of the flow). Refer to Caldeira and Sangra (2012) for a discussion on this topic.

Ocean surface kinetic energy (KE) also varies according to the wind forcing. Fig. 12 shows an increase in ocean KE up to 73% during the summer months for WRF forcing (red line), opposed to a weak surface KE when considering QuikSCAT forcing. Analyses of ocean surface vorticity (Fig. 13) show an increase

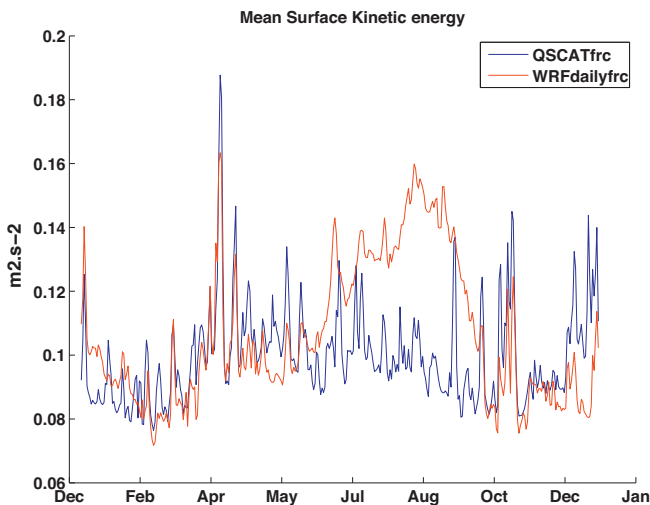


Fig. 12. Surface kinetic energy averaged over the domain represented in blue in Fig. 3. A strong increase occurs during the summer (June–September) when the model is forced by WRF. The peak in April occurring in both simulations can be related to the wind peak seen in Fig. 6 present in both wind product. (For interpretation of the references to color in this figure legend, the reader is referred to the web version of the article.)

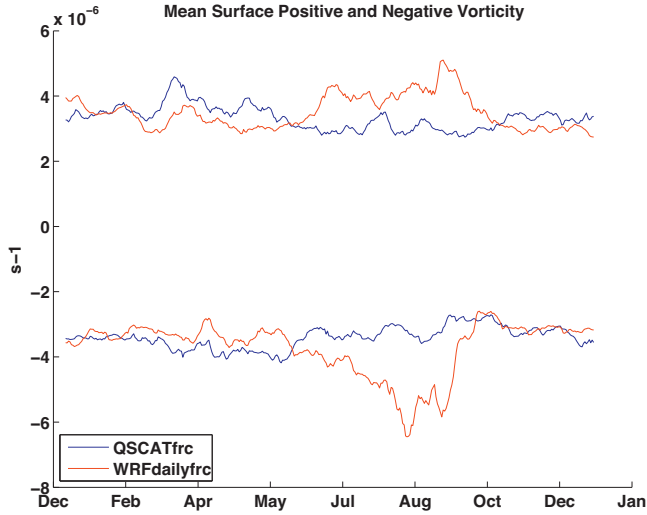


Fig. 13. Negative and positive vorticity spatially averaged over the domain represented in blue in Fig. 3. A net increase of both negative/positive vorticity is observed during the summer (June–September) period, suggesting the generation of eddies in the lee of Madeira. (For interpretation of the references to color in this figure legend, the reader is referred to the web version of the article.)

up to 75% of the positive and up to 103% of the negative vorticity during the summer months when using WRF as wind forcing.

In order to estimate the spatial repartition of the differences between the two cases, RMSD of the oceanic summer surface KE and of surface vorticity (normalized by planetary rotation f) were computed (Fig. 14). Large RMSD values are found south of Madeira and extend approximately 200 km downstream from the island (with a southwest orientation). RMSD values in the lee of Madeira could be explained by the local eddy generation, which would be consistent with eddies shedding downstream. As has been previously shown (Fig. 13), a stronger increase in negative (than in positive) vorticity and the shape of the RMSD wake (starting east of Madeira), suggest a predominance of wind-generated anticyclonic eddies. Wind curl asymmetries previously shown in the SAR images (Fig. 9) could also contribute to oceanic eddy asymmetries in the lee of Madeira as suggested by Caldeira and Sangra (2012).

In previous studies of eddy generation in the lee of Canary Islands (Sangra et al., 2009; Jimenez et al., 2008), the results were based on altimetry and/or numerical ocean models forced by analytically prescribed constant current and wind. This might have underestimated the generation of wind-induced eddies and overestimated the generation of eddies by flow-topography interaction. Altimetry derived products miss coastal regions and disregard the effect of the wind.

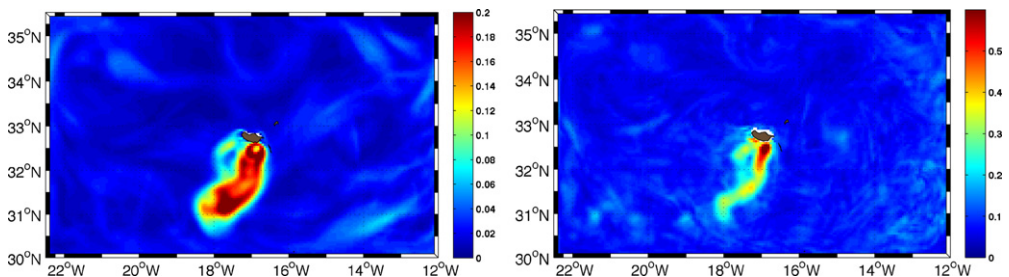


Fig. 14. Sea surface kinetic energy in $\text{m}^2 \text{s}^{-2}$ (left-panel) and vorticity normalized to f (right-panel) RMSD between WRF and QuikSCAT simulations for the summer period. Main differences are found south west of Madeira Archipelago.

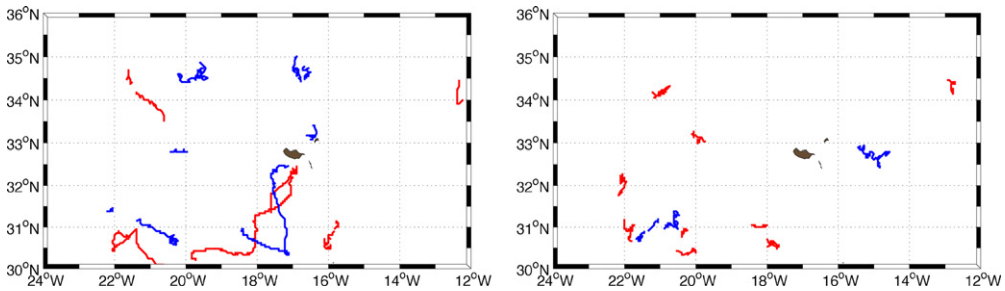


Fig. 15. Anticyclonic (red) and cyclonic (blue) eddy trajectories obtain from WRF (left-panel) and QuikSCAT (right-panel) forced simulation. Eddies generated before June and with lifetime inferior to 15 days are not represented. (For interpretation of the references to color in this figure legend, the reader is referred to the web version of the article.)

3.2.2. Eddy-containment in the lee of Madeira

The presence of eddies in the lee of Madeira is investigated using a Vector Geometry-Based Eddy Detection Algorithm from Nencioli et al. (2010) (cf. Section 2.4). Eddy trajectories identified in the 2008-ROMS solutions for both QuikSCAT and WRF forcing are shown in Fig. 15. Despite applying the eddy detection algorithm over the full year, only eddies generated during the summer (June–September) are discussed, withstanding that on the 31st December 2008 the two oldest eddies had not yet dissipated. For interpretation purposes, only eddies with a life time longer than 15 days are shown in Fig. 15.

In agreement with earlier results, no eddies were detected in the lee of Madeira when the model is forced using QuikSCAT wind. On the other hand when the ocean model is forced with WRF, three eddies are clearly identified. Two of these are anticyclonic and one is cyclonic. The anticyclonic eddies (hereafter named A1 and A2) have a life time of 208 and 44 days respectively, while the cyclonic one (hereafter named C) lived for at least 171 days. The longer-life-time anticyclonic eddy (A1) was first detected on the 19th of June traveling a distance of 622 km at a mean speed of 3.5 km/day. The cyclonic one was detected on the 1st of August and traveled a distance of 565 km at a mean speed of 3.7 km/day. The anticyclonic and the cyclonic eddies have a mean diameter of 49 km and 44.5 km respectively. These are under the detection limit of AVISO altimetry, which is estimated at 80 km (Chelton et al., 2007, 2011). It is therefore impossible to compare these finding to altimetry data.

Similarities between the trajectories of those eddies and the shape of the previous RMSD wake in Fig. 14 confirm that eddy shedding contributes to the downstream oceanic influence of the wind-wake.

Fig. 16 shows a sequence of images of surface vorticity (normalized by f) commencing with the first stage of detection of the first anticyclonic eddy (A1) to the end of the simulation (31st of December). It can be seen that the 2nd anticyclonic eddy (A2), which was detected on the 27 of August, only lived for 44 days before its merger with A1. It has been possible here to validate the eddies shape and trajectory determined by the eddy detector algorithm.

The Sangra et al. (2009) study of westward propagating eddies from the North Atlantic archipelagos was based on altimetry data. Nevertheless due to sensor limitations, AVISO altimetry data do not detect the early stages of eddy generation, i.e. sub-mesoscale eddy activity, particularly near coasts and islands. Therefore most Sangra et al. (2009) eddies drifting from Madeira Island were detected hundred miles westward from its coast. Results presented herein suggest that before propagating westward these island-induced eddies can be “trapped” in the wind-wake region, thus one can hypothesize that the early stages of the lifetime of these features is conditioned by the wind shear created by the wake before eddies join the westward propagating corridor described by Sangra et al. (2009) a few hundreds miles downstream.

To better understand the early life stage trajectory of eddies, we have considered the direct relation between wind direction, wind speed and eddy propagation. A link was found between zonal wind-shear ($\partial_x ws$, where ws is the wind speed) and eddy trajectory (Fig. 17). The anticyclonic eddy tends to follow the zonal wind-shear in its downstream trajectory before completely inflecting its trajectory

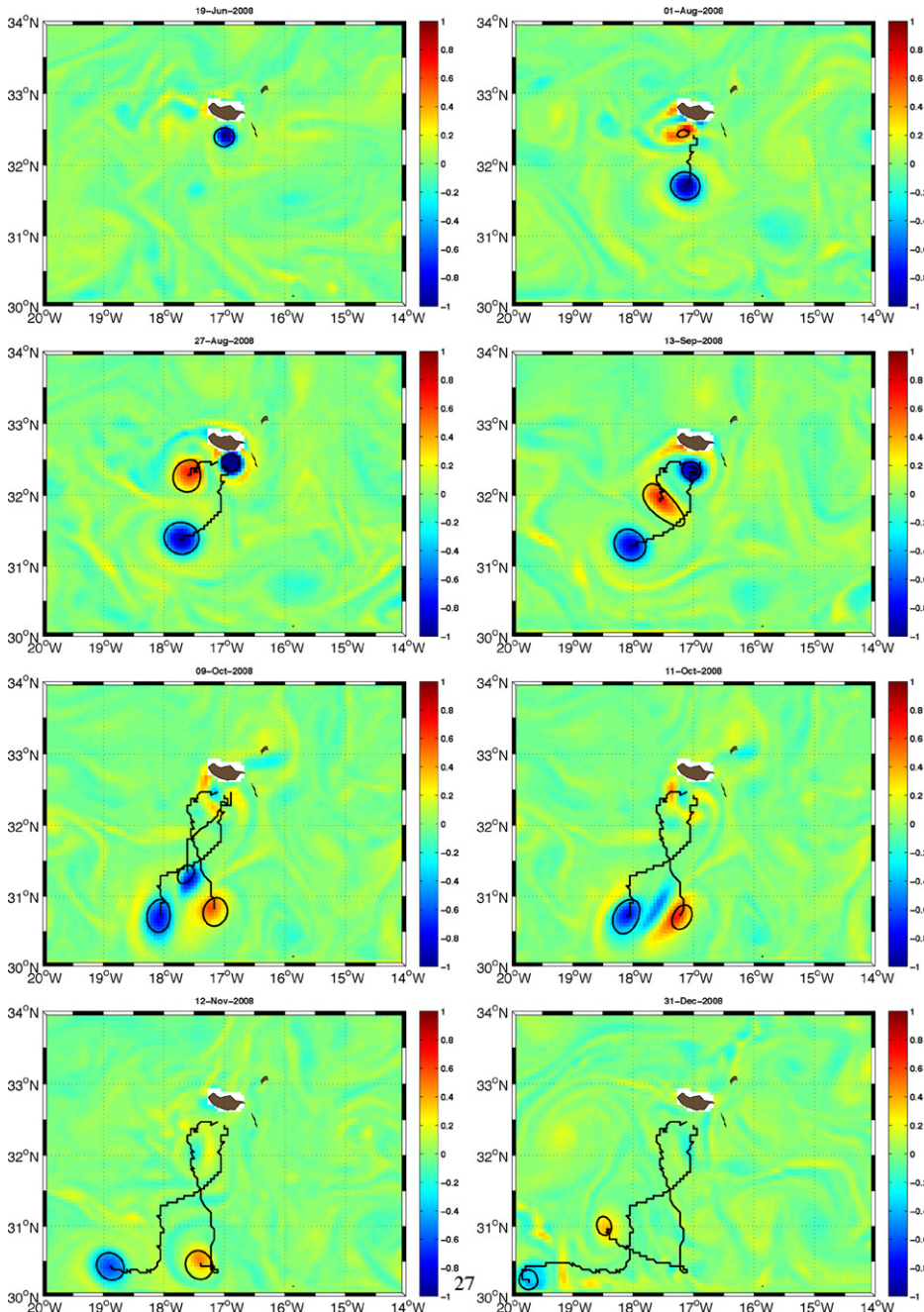


Fig. 16. ROMS sea surface vorticity (normalized by f): 19 June 2008 first detection of the anticyclonic eddy (A1); 1 August, first detection of the cyclonic eddy (C); 27 of August, first detection of the 2nd anticyclonic eddy (A2); 13 of September, intermediate stage; 9 October, last detection of A2; 11 October, A2 merging with A1; 12 November to 31 December, westward propagation of A1 and C. Eddy shapes (black circles) and center trajectories (black lines) were computed by the eddy tracking algorithm.

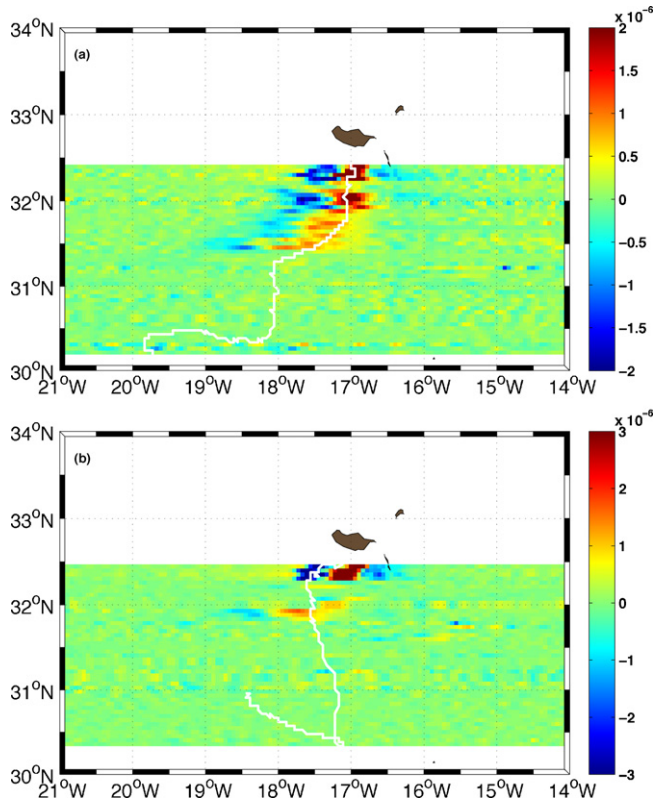


Fig. 17. Along track zonal wind shear given by $\partial_x ws$ where ws is the wind speed in m s^{-1} for an (top) anticyclonic eddy, and (bottom) cyclonic eddy. Black cross represent date of interest. 11 September to 18 October: A1–C interactions. 27 August to 10 October: A2–C interaction.

southward and later on westward. Fig. 17 shows along eddy track zonal wind-shear for A1 and C. To account for periods in which the eddies are either stationary or propagating in the zonal direction, zonal wind-shear has been averaged over such periods.

The anticyclonic eddy (Fig. 17(a)) starts by heading south following the positive zonal wind-shear up to 32°N , where its trajectory is inflected southwestward. Subsequently the eddy remained confined to the zonal wind-stress corridor until approximately 31.5°N , after which no more wind-induced influence is noticeable. The cyclonic eddy (Fig. 17(b)) has a southwest trajectory in its initial stage following the negative zonal wind-shear, then deflecting south at approximately 32.5°N having avoided the influence of the wind-shear. Although the cyclonic eddy was under the influence of the wind-shear containment for a shorter time periods, it is still interesting to note that both eddies were contained within the shear zone delimited by the east–west wind-jets. In previous discussions of island induced eddy containment, some authors have speculated that the wind might have influenced the organization and/or maintenance of these eddies downstream of islands, as witnessed by their high-frequency pulsation behavior (e.g. Nencioli et al., 2008; Sangra et al., 2009).

We hypothesize that the cyclonic eddy escaped from the wind influence because of interactions with both of the other eddies (A1 and A2). Thus C's inflecting trajectory to the South (Fig. 16) seems to coincide with the generation of A2 (27th of August). This could also explain why no relationship was found between eddy trajectory and zonal wind-shear for A2, which was interacting with C from its initial life stage, while A1 was not interacting with any other eddy and so allowing the wind trapping to act. Eddy–eddy interactions are difficult to predict and are left for future studies. They do seem to however give a good insight into the different ways eddies behave in relation to the wind trapping.

It seems probable that in the absence of eddy–eddy interactions, eddies tend to be trapped by the zonal wind shear of the wind–wake. Once free from those two constraints, the Beta effect might become responsible for the far field western Atlantic propagation, as suggested by Sangra et al. (2009) study of the NE Atlantic eddy–corridors.

It should be noted however that concomitant monitoring of high resolution atmospheric variables (e.g. wind) and oceanic vertical eddy characteristics is hard to accomplish in the field, especially when it is considered that mesoscale oceanic features can live for several months. Notwithstanding the difficulties, it is recommended that future studies should attempt to clarify the relative role of the near-field and far-field winds, planetary vorticity, background flows and vortex interactions throughout the lifetime and sometimes extensive travel of (sub)mesoscale eddy features.

4. Conclusions

In this study the oceanic impact of the Madeira atmospheric wake was assessed using wind products from two different sources. QuikSCAT was used to mimic a no-wind-wake scenario, whereas WRF calculated winds represented the island-induced change on the atmospheric flows, i.e. wind-wake. Both products were incorporated onto the ROMS ocean circulation model.

The main differences between these wind products were found near Madeira (near-field). Comparisons with high resolution winds extracted from SAR showed that WRF is able to realistically reproduce the Madeira wind-wake. Ocean surface vorticity and surface kinetic energy for the WRF forcing case, were observed to increase during strong wind-wake episodes that are dominant during the summer months.

It seems that in the absence of interactions between eddies, the wind-wake continues to manifest a strong influence in the downstream oceanic eddy propagation. Only after eddies are free from the wind-wake and from eddy–eddy interaction can they feel the earth rotation gradient (Beta) and start to propagate westward.

Future research should consider long-term simulations using a wider domain but at an equally moderate resolution, in order to continue to investigate these eddy-containment and eddy–eddy interaction phenomena.

In situ measurements are needed before major conclusions can be drawn. In addition to the continuous monitoring of atmospheric and oceanic variables in the near- and far-field wakes, future studies should consider the need for measurements at sufficient spatial and temporal resolutions.

Acknowledgments

The authors wish to acknowledge the two anonymous reviewers for their constructive comments, Alexandre Stegner for his interesting discussions and suggestions and Marcel Curé for his final edition of the text. Support for this research is provided from FCT-Portuguese National Science and Technology Foundation. This work was initiated in the scope of projects POCI/MAR/57265/2004 and PPCDT/MAR/57265/2004. Numerical model solutions were calculated at CIIMAR HPC unit, funded by the FCT pluriannual funds (PesT-C/MAR/LA0015/2011), and further expanded by funding from the RAlA.co project. SAR data were provided by ESA under project-6248 and derived wind product by CLS/SOPRANO (<http://soprano.cls.fr/>). QuikSCAT data were obtained from CERSAT (<http://cersat.ifremer.fr/>).

References

- Antonov, J.I., Locarnini, R.A., Boyer, T.P., Mishonov, A.V., Garcia, H.E., 2006. In: Levitus, S. (Ed.), *World Ocean Atlas 2005*, vol. 2: Salinity. NOAA Atlas NESDIS 62. Government Printing Office, Washington, DC, p. 182.
- Araújo, I.B., Caldeira, R.M.A., Couvelard, X., 2010. Island Induced (Sub) Mesoscale Features Around Madeira Archipelago (Initial Findings). Proceedings of the 3rd International workshop “SeaSAR 2010”, Frascati, January 2010. ESA SP-679 CD-ROM.
- Beckmann, A., Haidvogel, D., 1993. Numerical simulation of flow around a tall isolated seamount. Part I: Problem formulation and model accuracy. *J. Phys. Oceanogr.* 23, 1736–1753.
- Betts, A.K., 1986. A new convective adjustment scheme. Part I: Observational and theoretical basis. *Quart. J. Roy. Meteorol. Soc.* 112, 677–691.

- Betts, A.K., Miller, M.J., 1986. A new convective adjustment scheme. Part II: Single column tests using gate wave, bomex, and arctic air-mass data sets. *Quart. J. Roy. Meteorol. Soc.* 112, 693–709.
- Caldeira, R., Sangra, P., 2012. Complex geophysical wake flows. *Ocean Dyn.* 62, 785–797.
- Caldeira, R.M.A., Groom, S., Miller, P., Pilgrim, D., Nezlin, N., 2002. Sea-surface signatures of the island mass effect phenomena around Madeira Island, Northeast Atlantic. *Remote Sens. Environ.* 80, 336–360.
- Calil, P.H., Richards, K.J., Jia, Y., Bidigare, R.R., 2008. Eddy activity in the lee of the Hawaiian islands. *Deep Sea Res. Part II: Top. Stud. Oceanogr.* 55, 1179–1194.
- Chaigneau, A., Gizolme, A., Grados, C., 2008. Mesoscale eddies off Peru in altimeter records: identification algorithms and eddy spatio-temporal patterns. *Prog. Oceanogr.* 79, 106–119.
- Chelton, D.B., Freilich, M.H., Sienkiewicz, J.M., Ahn, J.V., 2006. On the use of QuikSCAT scatterometer measurements of surface winds for marine weather prediction. *Mon. Wea. Rev.* 134, 2055–2071.
- Chelton, D.B., deSzoeke, R.A., Schlax, M.G., El Naggar, K., Siwertz, N., 1998. Geographical variability of the first-baroclinic Rossby radius of deformation. *J. Phys. Oceanogr.* 28, 433–460.
- Chelton, D.B., Schlax, M.G., Samelson, R.M., 2011. Global observation of nonlinear mesoscale eddies. *Prog. Oceanogr.* 91, 167–216.
- Chelton, D.B., Schlax, M.G., Samelson, R., deSzoeke, R.A., 2007. Global observations of large oceanic eddies. *Geophys. Res. Lett.* 34.
- Chen, F., Dudhia, J., 2001. Coupling an advanced land-surface/ hydrology model with the Penn State/NCAR MM5 modeling system. Part I: Model description and implementation. *Mon. Wea. Rev.* 129, 569–585.
- Cushman-Roisin, B., 1994. *Introduction to Geophysical Fluid Dynamics*. Prentice-Hall, Inc., Upper Saddle River, New Jersey.
- Dee, D.P., Uppala, S.M., Simmons, A.J., Berrisford, P., Poli, P., Kobayashi, S., Andrae, U., Balmaseda, M.A., Balsamo, G., Bauer, P., Bechtold, P., Beljaars, A.C.M., van de Berg, L., Bidlot, J., Bormann, N., Delsol, C., Dragani, R., Fuentes, M., Geer, A.J., Haimberger, L., Healy, S.B., Hersbach, H., Hólm, E.V., Isaksen, I., Kållberg, P., Köhler, M., Matricardi, M., McNally, A.P., Monge-Sanz, B.M., Morcrette, J.J., Park, B.K., Peubey, C., de Rosnay, P., Tavolato, C., Thépaut, J.N., Vitart, F., 2011. The era-interim reanalysis: configuration and performance of the data assimilation system. *Quart. J. Roy. Meteorol. Soc.* 137, 553–597.
- Doglioli, A.M., Blanke, B., Speich, S., Lapeyre, G., 2007. Tracking coherent structures in a regional ocean model with wavelet analysis: application to cape basin eddies. *J. Geophys. Res.* 112, C05043, <http://dx.doi.org/10.1029/2006JC003952>.
- Dong, C.M., McWilliams, J.C., 2007. A numerical study of island wakes in the Southern California Bight. *Cont. Shelf Res.* 27, 1233–1248.
- Etling, D., 1989. On atmospheric vortex streets in the wake of large islands. *Meteorol. Atmos. Phys.* 41, 157–164.
- Fairall, C.W., Bradley, E.F., Hare, J.E., Grachev, A.A., Edson, J.B., 2003. Bulk parameterization of air–sea fluxes: updates and verification for the COARE algorithm. *J. Clim.* 16, 569–571.
- Hong, S.Y., Dudhia, J., Chen, S.H., 2004. A revised approach to ice microphysical processes for the bulk parameterization of clouds and precipitation. *Mon. Wea. Rev.* 132, 103–120.
- Janjic, Z.I., 1990. The step-mountain coordinate: physical package. *Mon. Wea. Rev.* 118, 1429–1443.
- Janjic, Z.I., 1994. The step-mountain eta coordinate model: further developments of the convection, viscous sublayer and turbulence closure schemes. *Mon. Wea. Rev.* 122, 927–945.
- Janjic, Z.I., 1996. The surface layer in the NCEP Eta model. In: *Eleventh Conference on Numerical Weather Prediction*, Norfolk, VA, 19–23 August; Amer. Meteor.
- Janjic, Z.I., 2000. Comments on development and evaluation of a convection scheme for use in climate models. *J. Atmos. Sci.* 57, 3686.
- Janjic, Z.I., 2002. Nonsingular implementation of the Mellor–Yamada level 2.5 scheme in the NCEP meso model. NCEP Office Note 437. NCEP.
- Jia, Y., Calil, P.H., Chassignet, E.P., Metzger, E.J., Potemra, J.T., Richards, K.J., Wallcraft, A.J., 2011. Generation of mesoscale eddies in the lee of the Hawaiian island. *J. Geophys. Res.*, 116.
- Jimenez, B., Sangra, P., Mason, E., 2008. A numerical study of the relative importance of wind and topographic forcing on oceanic eddy shedding by tall, deep water islands. *Ocean Model.* 22, 146–157.
- Kerboal, V., 2007. Improved bayesian wind vector retrieval scheme using ENVISAT ASAR data: principles and validation result. In: *ENVISAT Symposium*, Momtreux, Switzerland, 23–27 April 2007.
- Kersalé, M., Doglioli, A.M., Petrenko, A.A., 2011. Sensitivity study of the generation of mesoscale eddies in a numerical model of Hawaii islands. *Ocean Sci.* 7, 277–291.
- Large, W., McWilliams, J.C., Doney, S., 1994. Oceanic vertical mixing – a review and a model with no local boundary layer parameterization. *Rev. Geophys.* 32, 363–403.
- Lin, Y.L., Farley, R.D., Orville, H.D., 1983. Bulk parameterization of the snow field in a cloud model. *J. Clim. Appl. Meteorol.* 22, 1065–1092.
- Locarnini, R.A., Mishonov, A.V., Antonov, J.I., Boyer, T.P., Garcia, H.E., 2006. In: *Levitus, S. (Ed.), World Ocean Atlas 2005, vol. 1: Temperature*. NOAA Atlas NESDIS 61. U.S. Government Printing Office, Washington, DC, p. 182.
- Marchesiello, P., Debreu, L., Couvelard, X., 2009. Spurious diapycnal mixing in terrain-following coordinate models: the problem and a solution. *Ocean Model.* 26, 156–169.
- Marchesiello, P., McWilliams, J.C., Shchepetkin, A., 2001. Open boundary conditions for long-term integration of regional oceanic models. *Ocean Model.* 3, 1–20.
- Mlawer, E.J., Taubman, S.J., Brown, P.D., Iacono, M.J., Clough, S.A., 1997. Radiative transfer for inhomogeneous atmosphere: RRTM, a validated correlated-k model for the longwave. *J. Geophys. Res.* 104, 16663–16682.
- Moll, H.G., 1971. Die atmosphärische umströmung madeiras. *Beitr. Phys. Atmos.* 44, 227–244.
- Nencioli, F., Dong, C., Dickey, T.D., Washburn, L., McWilliams, J.C., 2010. A vector geometry-based eddy detection algorithm and its application to a high-resolution numerical model product and high-frequency radar surface velocities in the Southern California Bight. *J. Atmos. Oceanic Technol.* 27, 564–579.
- Nencioli, F., Kuwahara, V., Dickey, T.D., Rii, Y., Bidigare, R., 2008. Physical dynamics and biological implications of a mesoscale eddy in the lee of Hawaii: cyclone opal observations during E-Flux III. *Deep Sea Res. Part II: Top. Stud. Oceanogr.* 55, 1252–1274.

- Patzert, W., 1969. Eddies in Hawaiian waters. Tech. Rep. HIG-69-8. Hawaii Inst. of Geophys., Univ. of Hawaii at Manoa, Honolulu.
- Penven, P., Marchesiello, P., Debreu, L., Lefevre, J., 2007. Software tools for pre- and post-processing of oceanic regional simulations. *Environ. Model. Softw.* 23, 660–662.
- Piedeleu, M., Sangra, P., Sanchez-Vidal, A., Fabres, J., Gordo, C., Calafat, A., 2009. An observational study of oceanic eddy generation mechanisms by tall deep-water island (Gran Canaria). *Geophys. Res. Lett.*, 36.
- Portabella, M.A., Stoffelen, A., Johannessen, J.A., 2002. Toward an optimal inversion method for SAR wind retrieval. *J. Geophys. Res.*, 107.
- Pullen, J., Doyle, J.D., Haack, T., Dorman, C., Signell, R.P., Lee, C.M., 2007. Bora event variability and the role of air–sea feedback. *J. Geophys. Res.*, 112.
- Pullen, J., Doyle, J.D., May, P., Chavanne, C., Flament, P., Arnone, R.A., 2008. Monsoon surges trigger oceanic eddy formation and propagation in the lee of the Philippine Islands. *Geophys. Res. Lett.* 35.
- Pullen, J., Doyle, J.D., Signell, R.P., 2005. Two-way air–sea coupling: a study of the Adriatic. *Mon. Wea. Rev.*, 1–49.
- Sangra, P., Pascual, A., Rodriguez-Santana, A., Machin, F., Mason, E., McWilliams, J.C., Pelegri, J.L., Dong, C.M., Rubio, A., Aristegui, J., Marrero-Diaz, A., Hernandez-Guerra, A., Martinez-Marrero, A., Auladell, M., 2009. The canary eddy corridor: a major pathway for long-lived eddies in the subtropical north Atlantic. *Deep Sea Res. Part I: Oceanogr. Res. Pap.* 56, 2100–2114.
- Scorer, R.S., 1986. *Cloud Investigation by Satellite*. John Wiley, New York (chapter Cloud investigation by satellite).
- Shchepetkin, A.F., McWilliams, J.C., 1998. Quasi-monotone advection schemes based on explicit locally adaptive dissipation. *Mon. Wea. Rev.*, 1541–1580.
- Shchepetkin, A.F., McWilliams, J.C., 2003. A method for computing horizontal pressure-gradient force in an oceanic model with a nonaligned vertical coordinate. *J. Geophys. Res.-Oceans*, 108.
- Shchepetkin, A.F., McWilliams, J.C., 2005. The regional oceanic modeling system (ROMS): a split-explicit, free-surface, topography-following-coordinate oceanic model. *Ocean Model.* 9, 347–404.
- Signell, R.P., Chiggiato, J., Horstmann, J., Doyle, J.D., Pullen, J., Askari, F., 2010. High-resolution mapping of Bora winds in the northern Adriatic sea using synthetic aperture radar. *J. Geophys. Res.-Oceans* 115, C04020.
- Skamarock, W.C., Klemp, J.B., Dudhia, J., Gill, D., Barker, D., Wang, W., Powers, J., 2008. A description of the Advanced Research WRF Version 3. NCAR Tech Note NCAR TN-475-STR. NCAR.
- Small, R., deSzoeko, S., Xie, S., O'Neill, L., Seo, H., Song, Q., Cornillon, P., Spall, M.A., Minobe, S., 2008. Air–sea interaction over ocean fronts and eddies. *Dyn. Atmos. Oceans* 45, 274–319.
- Song, Y., Haidvogel, D., 1994. A semi-implicit circulation model using a generalized topography-following coordinate system. *J. Comput. Phys.* 115, 228–244.
- Stoffelen, A., Anderson, D., 1997. Scatterometer data interpretation: estimation and validation of the transfer function CMOD4. *J. Geophys. Res.* 102, 5767–5780.
- Yoshida, S., Qiu, B., Hacker, P., 2010. Wind-generated eddy characteristics in the lee of the island of Hawaii. *J. Geophys. Res.-Oceans*, 115.